

## DISK FORMATION ENABLED BY ENHANCED RESISTIVITY

RUBEN KRASNOPOLSKY<sup>1,2</sup>, ZHI-YUN LI<sup>3,2</sup>, HSIEN SHANG<sup>1,2</sup>

*Submitted to ApJ 2009 October 21; accepted 2010 April 2*

### ABSTRACT

Disk formation in magnetized cloud cores is hindered by magnetic braking. Previous work has shown that for realistic levels of core magnetization, the magnetic field suppresses the formation of rotationally supported disks during the protostellar mass accretion phase of low-mass star formation both in the ideal MHD limit and in the presence of ambipolar diffusion for typical rates of cosmic ray ionization. Additional effects, such as ohmic dissipation, the Hall effect, and protostellar outflow, are needed to weaken the magnetic braking and enable the formation of persistent, rotationally supported, protostellar disks. In this paper, we first demonstrate that the classic microscopic resistivity is not large enough to enable disk formation by itself. We then experiment with a set of enhanced values for the resistivity in the range  $\eta = 10^{17} - 10^{22} \text{ cm}^2 \text{ s}^{-1}$ . We find that a value of order  $10^{19} \text{ cm}^2 \text{ s}^{-1}$  is needed to enable the formation of a  $10^2$  AU-scale Keplerian disk; the value depends somewhat on the degree of core magnetization. The required resistivity is a few orders of magnitude larger than the classic microscopic values. Whether it can be achieved naturally during protostellar collapse remains to be determined.

*Subject headings:* accretion, accretion disks — ISM: clouds — ISM: magnetic fields — magnetohydrodynamics (MHD)

### 1. INTRODUCTION

#### 1.1. Magnetic Braking and Disk Formation

Circumstellar disks play a central role in both star and planet formation. The disks are thought to be the conduit through which Sun-like stars assemble the bulk of their mass (Shu, Adams, & Lizano 1987). They are also the birthplace of planets. Despite years of active research (see reviews by Bodenheimer 1995 for early work), we still do not have answers to some of the most basic questions, such as “when and how does a disk appear in the process of star formation?”

Observationally, it is difficult to separate out the protostellar disk from the surrounding envelope during the early, embedded phase of star formation with the current generation of interferometers (e.g., Jørgensen et al. 2007), although the situation will improve drastically in a few years, when ALMA comes online (van Dishoeck & Jørgensen 2008). Enoch et al. (2009) inferred the existence of a large (hundreds of AU in radius), massive (more than  $0.1 M_{\odot}$ ) disk around the protostar Serpens FIRS 1, based mostly on CARMA dust continuum observations. Without a detailed knowledge of the central stellar mass and gas kinematics on small (arcsec) scales, it is difficult to determine whether the inferred structure is a rotationally supported disk, a magnetically induced “pseudodisk,” or simply the inner part of an envelope that is dynamically more complicated than the Ulrich’s (1976) rotating, collapsing sphere adopted by Enoch et al. (2009) for the protostellar envelope. Theoretically, disk formation in dense cores of molecular clouds magnetized to the observed level (corresponding to a mean

dimensionless mass-to-flux ratio  $\lambda \sim$  a few; Troland & Crutcher 2008) is controlled by magnetic braking, which has been difficult to quantify until recently.

Detailed calculations have now shown that the magnetic braking is apparently so efficient as to inhibit the formation of rotationally supported disks *during the main protostellar accretion phase* for a moderate level of core magnetization, as long as the magnetic field is frozen in the matter (i.e., the ideal MHD limit; Allen, Li, & Shu 2003; Galli et al. 2006; Price & Bate 2007; Hennebelle & Fromang 2008; Mellon & Li 2008; see, however, Hennebelle & Ciardi 2009 for a different view, and also Machida et al. 2005 and Banerjee & Pudritz 2006 for the evolution of rotating, magnetized cores prior to the main accretion phase). In order for a rotationally supported disk to exist around a rapidly accreting protostar, the magnetic braking must be weakened one way or another. The most obvious possibility is through non-ideal MHD effects, which are expected to be important in lightly ionized star-forming cores. However, we have recently shown that ambipolar diffusion, the best studied non-ideal MHD effect in star formation, does not sufficiently weaken the braking to allow rotationally supported disks to form for realistic levels of core magnetization and ionization; in some cases, the magnetic braking is even enhanced (Mellon & Li 2009, Krasnopolsky & Königl 2002; see Basu & Mouschovias 1995, Hosking & Whitworth 2004 and Duffin & Pudritz 2009, who considered the effects of ambipolar diffusion on magnetic braking and core fragmentation during the earlier phase of prestellar core evolution). This motivates us to examine whether two of the remaining non-ideal MHD effects, ohmic dissipation and the Hall effect, can weaken the coupling between the magnetic field and the bulk neutral matter (and thus the strength of magnetic braking) enough to enable the formation of rotationally supported disks. This paper concentrates on the ohmic dissipation.

<sup>1</sup> Academia Sinica, Institute of Astronomy and Astrophysics, Taipei, Taiwan

<sup>2</sup> Academia Sinica, Theoretical Institute for Advanced Research in Astrophysics, Taipei, Taiwan

<sup>3</sup> University of Virginia, Astronomy Department, Charlottesville, USA

### 1.2. Electrical Resistivity of Cloud Cores

The resistivity  $\eta$  is related to the electrical conductivity  $\sigma$  through

$$\eta = \frac{c^2}{4\pi\sigma} . \quad (1)$$

For lightly ionized molecular gas in dense cores, the electric conductivity is usually dominated by the contribution from electrons, although the grain contribution can dominate at high densities when large amounts of small grains are present (e.g., Wardle & Ng 1999). To obtain a rough estimate for the conductivity, we will concentrate on the contribution from the electrons, which is given by

$$\sigma_e = \frac{n_e e^2 m_{\text{H}_2}}{m_e \rho \langle \sigma v \rangle_{e-\text{H}_2}} = 9.0 \times 10^{16} x_e \text{ (s}^{-1}\text{)} , \quad (2)$$

where  $\rho = 2.8 m_{\text{H}} n_{\text{H}_2}$  and  $x_e = n_e/n_{\text{H}_2}$ . We have adopted a value  $\langle \sigma v \rangle_{e-\text{H}_2} = 2 \times 10^{-9} \text{ cm}^3 \text{ s}^{-1}$  for a 10 K gas from Pinto & Galli (2008). This value is somewhat smaller than that used in Draine et al. (1983) and Wardle & Ng (1999), which is  $2.6 \times 10^{-9} \text{ cm}^3 \text{ s}^{-1}$ , but somewhat larger than that of Sano et al. (2000), which is  $1.3 \times 10^{-9} \text{ cm}^3 \text{ s}^{-1}$ . It increases slowly with temperature, roughly as  $T^{1/2}$ , yielding a lower resistivity at a higher temperature. Since our calculation is assumed to be isothermal, the temperature dependence is not used.

Substituting equation (2) into equation (1) yields

$$\eta = \frac{7.9 \times 10^{22}}{x_e} \text{ (cm}^2 \text{ s}^{-1}\text{)} . \quad (3)$$

The fractional ionization  $x_e$  can be computed from detailed chemical networks. At the relatively high densities that are relevant for disk formation, it depends on the grain size distribution. For the standard Mathis, Rumpl, & Nordsieck (1977) distribution, Nakano, Nishi, & Umebayashi (2002) computed the ionization fraction over a large range of number density (their Figure 1). Over the critical range of density  $\sim 10^8\text{--}10^{12} \text{ cm}^{-3}$  where the transition between the rapidly infalling pseudodisk<sup>4</sup> and a potential Keplerian disk is expected to occur, the fraction can be fitted roughly by

$$x_e \approx 10^{-14} \left( \frac{10^{10} \text{ cm}^{-3}}{n_{\text{H}_2}} \right) , \quad (4)$$

which corresponds to a resistivity of

$$\eta = 1.7 \times 10^{17} \left( \frac{\rho}{10^{-13} \text{ g cm}^{-3}} \right) \text{ (cm}^2 \text{ s}^{-1}\text{)} . \quad (5)$$

The fit of fractional ionization deviates substantially from the computed values at low densities. However, the deviation is expected to be inconsequential because the low density envelope is sufficiently ionized to be close to the ideal MHD limit (ignoring ambipolar diffusion, which is investigated separately elsewhere, see e.g., Krasnopolsky & Königl 2002 and Mellon & Li 2009) according to either equation (4) or the computed values. If only relatively large grains of size (of order  $0.1 \mu\text{m}$ ) exist, the ionization fraction would be higher (by as much as

three orders of magnitude, see Figure 1 of Umebayashi & Nakano 1990, or compare Figures 1 and 3 of Wardle & Ng 1999), making the resistivity smaller. Equation (5) should therefore be viewed as a rough indication of the plausible upper range of the “classic” (as opposed to “anomalous”) resistivity, especially in view of the fact that the actual temperature in the high density region of disk formation is expected to be higher than the 10 K adopted in our calculation, which would lower the resistivity. It may be enhanced, however, through anomalous processes (e.g., Norman & Heyvaerts 1985).

The rest of the paper is organized as follows. In §2, we describe the setup of the disk formation problem, focusing on the protostellar mass accretion phase, when a central object has formed. For illustrative purposes, we will concentrate on a particular set of core parameters for which a  $10^2$  AU-scale disk is formed at a representative time  $t = 10^{12}$  s (or about  $3 \times 10^4$  yr) in the absence of magnetic braking, and a magnetic field that is strong enough to suppress the formation of a rotationally supported disk in the ideal MHD limit. We consider in §3 whether the illustrative classic resistivity given in equation (5) can weaken the magnetic braking enough to enable disk formation, and find that the answer is no. In §4, we explore the question of how large the resistivity must be in order for the  $10^2$  AU-scale rotationally supported disk to reappear in our model problem. It turns out to be of order  $10^{19} \text{ cm}^2 \text{ s}^{-1}$ , a few orders of magnitude larger than the classic value expected on the  $10^2$  AU-scale, as anticipated by Shu et al. (2006) based on the concept of the so-called Ohm sphere, although our value is one to two orders of magnitudes smaller than theirs, depending on the field strength. The numerical results and their astrophysical implications are discussed in the last section, §6.

## 2. PROBLEM SETUP

Our primary goal is to illustrate the effects of ohmic dissipation on magnetic braking and disk formation. For this purpose, it is desirable to have as small a numerical magnetic diffusivity as possible, which demands a high spatial resolution. High resolution, however, puts a stringent limit on the computation time step  $dt$ , which is proportional to the square of the (smallest) grid size for the explicit method that we use to treat the ohmic dissipation. Although subcycling can be used to alleviate the time step problem substantially, a large number of cycles are still needed to reach a reasonable protostellar accretion time, say,  $10^{12}$  s, making the treatment of self-gravity difficult. For this initial exploration of the effects of ohmic dissipation, we have decided to set up a simplified disk formation problem, with a rotating, non-self-gravitating envelope falling onto a central object of fixed mass  $M_*$ . It will turn out that a large “anomalous” resistivity is needed to save the disk, an elaborate disk formation model is probably not warranted at this early stage of the investigation.

Specifically, we solve the equations of resistive MHD,

$$\frac{\partial \rho}{\partial t} + \nabla \cdot (\rho \mathbf{v}) = 0 , \quad (6)$$

$$\frac{\partial \mathbf{v}}{\partial t} + (\mathbf{v} \cdot \nabla) \mathbf{v} = -\frac{\nabla p}{\rho} + \frac{\mathbf{J} \times \mathbf{B}}{\rho c} - \nabla \Phi_g , \quad (7)$$

<sup>4</sup> By “pseudodisk” we mean in this paper a structure formed by the magnetically induced flattening of infalling material due to anisotropic magnetic forces, as in Galli & Shu (1993).

$$4\pi\mathbf{J} = c\nabla \times \mathbf{B}, \quad (8)$$

$$\frac{\partial \mathbf{B}}{\partial t} = \nabla \times (\mathbf{v} \times \mathbf{B} - \eta \nabla \times \mathbf{B}) \quad (9)$$

under the assumption of axisymmetry, and adopt a spherical polar coordinate system  $(r, \theta, \phi)$ , with a stellar object of  $M_* = 0.5M_\odot$  at the origin such that the gravitational potential is  $\Phi_g = -GM_*/r$ , neglecting the self-gravity of the gas. Self-gravity will be included in a follow-up work, where we will evolve the magnetized core from its formation to collapse in a self-consistent manner. For this initial study, we aim to capture the essence of the problem of magnetic suppression of disk formation in the simplest possible way, by adopting uniform distributions for the initial gas density and magnetic field, and to study the effects of a new ingredient, resistivity, in this simplest problem.

At time  $t = 0$ , we fill the computation domain between  $r_i = 1.5 \times 10^{14}$  cm and  $r_o = 1.5 \times 10^{17}$  cm with a uniform density  $\rho_0 = 1.4 \times 10^{-19}$  g cm $^{-3}$  (corresponding to  $n(\text{H}_2) = 3.0 \times 10^4$  cm $^{-3}$ ), so that the total envelope mass is  $1M_\odot$ . For simplicity, we assume that the gas stays isothermal, with an isothermal sound speed  $a = (p/\rho)^{1/2} = 2 \times 10^4$  cm s $^{-1}$  (corresponding to a temperature of about 10 K). For the initial rotation, we adopt the following prescription:

$$v_\phi = v_{\phi,0} \tanh(\varpi/\varpi_c) \quad (10)$$

where we choose  $v_{\phi,0} = 2 \times 10^4$  cm s $^{-1}$ ,  $\varpi$  is the cylindrical radius, and  $\varpi_c = 3 \times 10^{15}$  cm. The softening of the rotational profile inside the cylindrical radius  $\varpi_c$  is to prevent the angular speed from becoming singular near the rotation axis. Since the inner radius of our computational domain is 10 AU, we are concerned with the formation or suppression of relatively large disks (of tens of AU or more) only. Our initial rotation is relatively fast: Goodman et al. (1993) estimated observationally that the ratio of rotational to gravitational energies for dense  $\text{NH}_3$  cores is typically  $\sim 0.02$ , which would imply  $v_\phi \sim 3 \times 10^3$  cm s $^{-1}$  for our setup. Our choice of a faster rotational speed is conservative in that it is harder to remove a larger initial angular momentum through magnetic braking (see also Mellon & Li 2008).

The calculations are done with a new version of Zeus, dubbed “ZeusTW”. ZeusTW, written in idiomatic Fortran95, is based on the “Zeus36” code (Krasnopolsky, Li, & Blandford 1999, 2003), itself derived from Zeus3D (LCA version 3.4.2: Clarke, Norman, & Fiedler 1994); Zeus36 is parallel by domain decomposition, and utilizes dynamic memory for its field and grid arrays. A small memory pool of temporary arrays replaces the worker arrays of Zeus3D, increasing programming flexibility at essentially zero runtime cost. ZeusTW adds to Zeus36 the ability to solve many non-ideal MHD problems in an explicit form, covering the ohmic, Hall, and ambipolar diffusion terms. To treat the ohmic term relevant for this paper, we used a resistivity algorithm based on Fleming, Stone, & Hawley (2000), which includes subcycling. We tested the code by diffusing an initial Gaussian profile in Cartesian geometry, in one, two, and three dimensions. We also tested slightly different forms of the algorithm (such as changing the operator splitting by calculating the current density  $\mathbf{J}$  before or after the magnetic field  $\mathbf{B}$

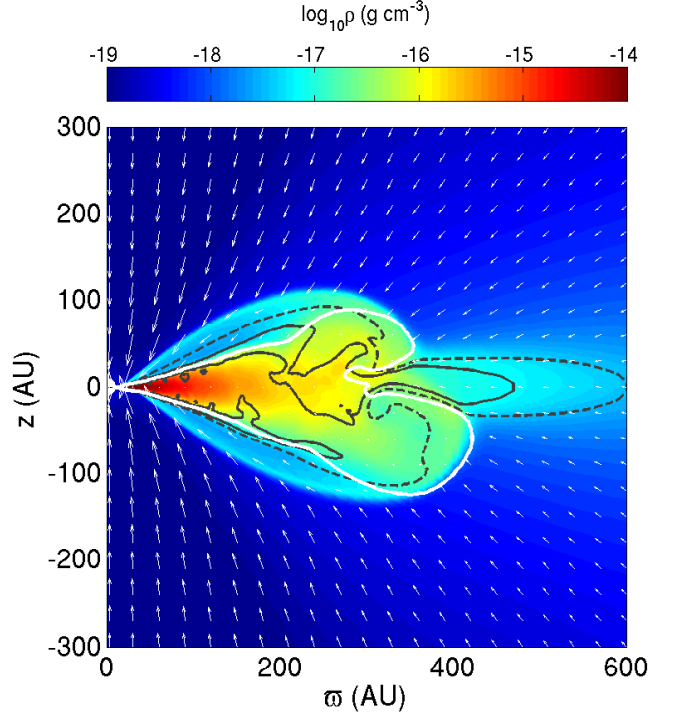


**Figure 1.** Snapshot of the rotationally supported disk formed in the absence of magnetic braking at a representative time  $t = 10^{12}$  s. Logarithm of density (colormap); radial infall sonic transition  $v_r = -a = -2 \times 10^4$  cm s $^{-1}$  (white line); poloidal velocity field (arrows, scale can be estimated from the radial infall component at the white line); and level of Keplerian support  $|v_\phi/v_K|$  (dark gray dashes at 90% and solid line at 100%), where  $v_K = (GM_*/\varpi)^{1/2}$ .

is updated), and different subcycling prescriptions (such as varying the maximum number of ohmic subcycles from 1 to 100). The code passed all of these tests.

### 2.1. Disk Formation in the Non-Magnetic Case

We adopt the standard hydro outflow boundary conditions at both the inner and outer (radial) boundaries of the computation domain (these boundary conditions impose continuity of material outflowing the grid, helping to reduce artificial reflections of waves at boundaries). We use 400 non-uniformly spaced grid points in the radial direction, corresponding to a smallest radial grid size  $dr_{\min} = 3 \times 10^{12}$  cm (or 0.2 AU) and a ratio of adjacent zone sizes of 1.017. We use 180 uniform zones in the  $\theta$  direction, corresponding to a minimum polar grid size of  $2.6 \times 10^{12}$  cm, comparable to the smallest radial grid size. With this setup, we obtain a rotationally supported disk of radius  $r_d \approx 400$  AU and mass  $m_d \approx 0.01M_\odot$  at a time  $t = 10^{12}$  s in the absence of magnetic braking; the time is comparable to the duration of the deeply embedded Class 0 phase (André et al. 2000, see, however, Evans et al. 2009 who concluded that the duration is longer). A snapshot of the disk is shown in Figure 1. The hydrodynamic disk is resolved in the radial direction by more than 200 zones. We have experimented with coarser grids (e.g., a total of 200 radial zones and 90 angular zones), finding qualitatively similar results, which indicates that the resolution employed is sufficient. An example of the lower resolution runs is shown in §4 below.

The disk size at  $t = 10^{12}$  s can be understood roughly as follows. We first estimate the radius of the infall re-

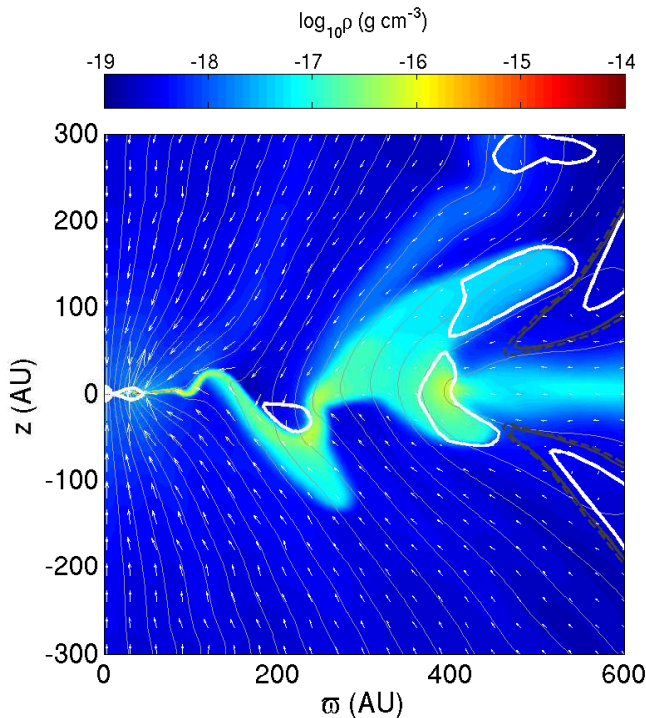


**Figure 2.** Same as Figure 1 but for the ideal MHD model. The field lines are drawn as thin solid lines (20 contour lines of magnetic flux, with flux levels quadratically spaced from zero at the axis up to the flux value at the outer equator point of each magnetized figure). The field component  $B_z$  is  $470 \mu\text{G}$  at the center of the figure. No rotationally supported structure forms in this simulation, although the flow structure is strongly affected by numerical reconnection of field lines.

gion  $r$  at time  $t$ , and the specific angular momentum  $\ell$  of the material at that radius. Assuming that pressure gradients are negligible compared to the central gravity, we have the infall speed at any given radius to be near the free fall value  $v(r) = (2GM_*/r)^{1/2}$ . The infall radius is then roughly  $t \sim r/v \sim r^{3/2}/(2GM_*)^{1/2}$ , which yields  $r \sim 5 \times 10^{16} \text{ cm}$  at  $t = 10^{12} \text{ s}$ , much larger than  $\varpi_c$  (the characteristic radius for rotation initial profile change). Therefore, the equatorial material at radius  $r$  has a specific angular momentum of  $\ell = rv = r \times 2 \times 10^4 \text{ cm s}^{-1}$ . Conservation of angular momentum around a star of mass  $0.5M_\odot$  tells us that the specific angular momentum corresponds to a centrifugal radius of  $\sim 1000 \text{ AU}$ , which is about a factor of 2 larger than our numerically obtained disk radius  $\sim 400 \text{ AU}$ . We consider the agreement satisfactory, given the crudeness of the infall estimate, and the fact that most material on the surface of the infall sphere at radius  $r$  has a specific angular momentum  $\ell$  less than the above estimate (valid only for the equatorial region), and the centrifugal radius is sensitive to  $\ell$  (as  $\ell^2$ ).

### 2.2. Suppression of Disk Formation in the Ideal MHD Limit

As mentioned in §1, previous studies have shown that a moderate magnetic field corresponding to a dimensionless mass-to-flux ratio of a few can completely suppress the formation of rotationally supported disks in the ideal MHD limit (at least when the rotation and magnetic axes are aligned; see Hennebelle & Ciardi 2009). Even though

the mass-to-flux ratio is ill-defined in our current model setup that does not include the self-gravity of the envelope gas, we find that the disk formation can still be suppressed if the magnetic field is strong enough. An example is shown in Figure 2, where the initially uniform mass distribution in the computational domain of the hydro model shown in Figure 1 is threaded with a uniform magnetic field  $B_0 = \sqrt{4\pi} \times 10 \mu\text{G} \approx 35 \mu\text{G}$  along the rotation axis. The field strength is in the range inferred by Troland & Crutcher (2008) for a sample of dark cloud cores, after correcting for projection effects. For comparison, we also considered a weaker field of  $B_0 = \sqrt{4\pi} \times 3 \mu\text{G} \approx 10.6 \mu\text{G}$  and obtained qualitatively similar results. For MHD calculations, we adopt the standard outflow boundary condition for the magnetic field at the outer radial boundary, and a torque-free (i.e.,  $B_\phi = 0$ ) outflow boundary condition at the inner radial boundary, as in Mellon & Li (2008).

The flow structure is strongly affected by numerical reconnection of the field lines. The reconnection is an unavoidable consequence of the dragging of the field lines into a highly pinched, split-monopole type configuration by gravitational collapse in the ideal MHD limit (Galli et al. 2006). The build up of magnetic flux in the central region as a result of continuous mass accretion forces the oppositely directed field lines above and below the equator closer and closer together, eventually triggering (numerical) reconnection. It is present in other ideal MHD calculations of magnetized core collapse, such as Mellon & Li (2008). Because of the (unavoidable) numerical artifacts, it is difficult to quantify the exact strength of the magnetic braking. Nevertheless, it is clear from Figure 2 that a coherent disk does not exist; it is replaced by a set of dense blobs, which are not rotationally supported (and may break up asymmetrically in 3D). The prominent dense blobs and sheets at radii 400 AU and smaller are all rotating well below their local Keplerian speed (especially the innermost ones), as can be seen from the thick dashed and solid dark gray lines at radii greater than  $\varpi \sim 400 \text{ AU}$  in Figure 2, which mark the location of  $|v_\phi| = 0.9v_K$  and  $v_K$ , respectively ( $v_K$  is the local Keplerian speed). The blobs and sheets are supported to a large extent by the magnetic tension force from the pinched field lines.

### 3. INABILITY FOR CLASSIC RESISTIVITY TO ENABLE DISK FORMATION

We now address the question of whether the illustrative classic resistivity given in Equation (5) can weaken the magnetic braking enough to enable the formation of rotationally supported disks or not. For this purpose, we have implemented into the MHD code ZeusTW an explicit treatment of resistivity, following the work of Fleming, Stone, & Hawley (2000) and Miller & Stone (1997; see also Fendt & Čemeljić 2002). In these treatments, the resistive term of the induction equation is included through operator splitting, respecting the constrained transport condition that keeps the field divergence null to machine round-off. Numerical stability of this term limits the timestep  $\Delta t_\Omega$  to a value  $\propto (\Delta x)^2$ , a quadratic requirement that can be much more stringent than the time  $\Delta t_{\text{IMHD}} \propto (\Delta x)^1$  required for treating the hydrodynamics and the ideal MHD terms. Fortunately, the resistive term is computationally inexpensive com-



**Table 1**  
Model Characteristics

Model	$B_0(\mu\text{G})$	$\eta$	Disk	Notes
HD	0	no	yes	Hydro simulation
IMHD	35.4	no	no	Ideal MHD
CR	35.4	yes	no	Classic resistivity given by Eq. (5)
ER18	35.4	yes	no	Enhanced resistivity $\eta = 10^{18}$
ER18.5	35.4	yes	no	Enhanced resistivity $\eta = 3 \times 10^{18}$
ER19	35.4	yes	no	Enhanced resistivity $\eta = 10^{19}$
ER19.5	35.4	yes	yes	Enhanced resistivity $\eta = 3 \times 10^{19}$
ER20	35.4	yes	yes	Enhanced resistivity $\eta = 10^{20}$
IMHDw	10.6	no	no	Weaker field, ideal MHD
ER18w	10.6	yes	no	Weaker field, $\eta = 10^{18}$
ER18.5w	10.6	yes	yes	Weaker field, $\eta = 3 \times 10^{18}$
ER19w	10.6	yes	yes	Weaker field, $\eta = 10^{19}$
ER19.5w	10.6	yes	yes	Weaker field, $\eta = 3 \times 10^{19}$
ER20w	10.6	yes	yes	Weaker field, $\eta = 10^{20}$

NOTE — “Disk” in column 4 refers to “rotationally supported disk” at time  $t = 10^{12}$  s. Enhanced resistivities  $\eta$  are given in cgs units ( $\text{cm}^2 \text{s}^{-1}$ ).

pared to the rest of the induction equation, and so it can be efficiently subcycled. We have checked that subcycling speeds up the calculations typically by a substantial factor and does not change the results significantly. We have also tried small changes in the operator splitting scheme, such as altering the order of the ideal MHD and the resistivity terms, or adding both terms together. These changes had no substantial effect on the results, and therefore we chose the scheme that was most convenient for efficient subcycling, which is one identical to that used in Fleming, Stone, & Hawley (2000).

Figure 3 displays a snapshot of the simulation at the representative time  $10^{12}$  s. A dense flattened structure develops in the inner equatorial region. It is, however, fragmented as in the ideal MHD case, indicating that the classic resistivity is too small to completely suppress the numerical reconnection of field lines. The dense blob at radius  $\sim 400$  AU, in particular, is similar to the outermost blob in Figure 2, and is due to an early reconnection event. The artificial reconnection events make it difficult to carry out detailed analysis. Nevertheless, it is easy to show that the dynamics of the inner equatorial region is far from that of a rotationally supported disk. First, the equatorial material inside  $\sim 400$  AU is often counter-rotating, with a rotation speed that sometimes decreases toward the center (rather than increasing as would be expected for a Keplerian disk: see Figure 4). Second, the radial motion in the region is mostly supersonic ( $> 2 \times 10^4 \text{ cm s}^{-1}$ ). The rapid infall is an indication that the dense, flattened structure is a magnetically produced pseudodisk (Galli & Shu 1993), rather than a rotationally supported Keplerian disk. There is one region of supersonic outflow at  $\sim 50$  AU. This region, and other outflow events that appeared during the simulation, are related to episodic reconnection events, as in the ideal MHD model. In any case, classic resistivity does not appear capable of weakening magnetic braking enough to enable the formation of a rotationally supported disk. Enhanced resistivity is needed if ohmic dissipation is to save the disk.

#### 4. ENHANCED RESISTIVITY AND DISK FORMATION

It is well known that anomalous resistivity orders of magnitude larger than the classic value is required to

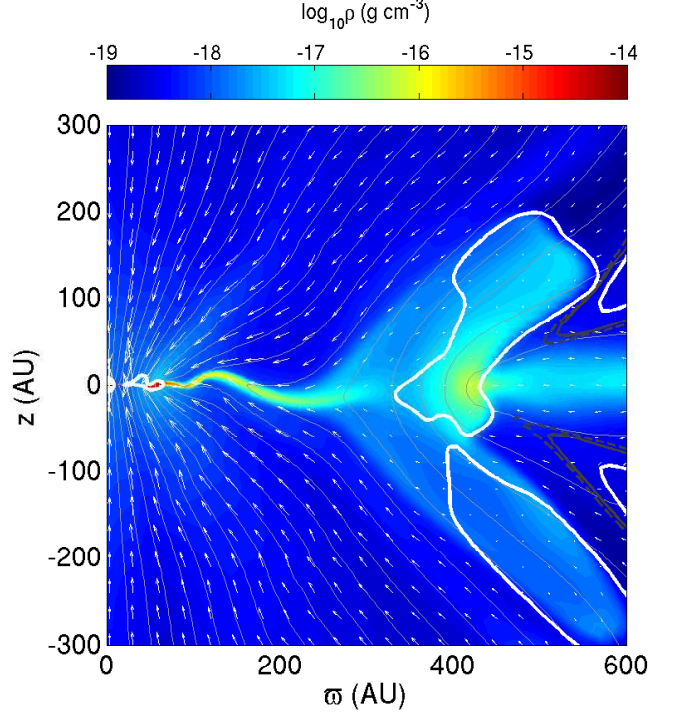


**Figure 3.** Same as Figures 1 and 2 but for the MHD model with the classic resistivity given in Equation (5). A dense, flattened structure exists near the equator, but it is a highly dynamic magnetically produced pseudodisk rather than a rotationally supported disk. The flow structure is affected by numerical reconnection of field lines.

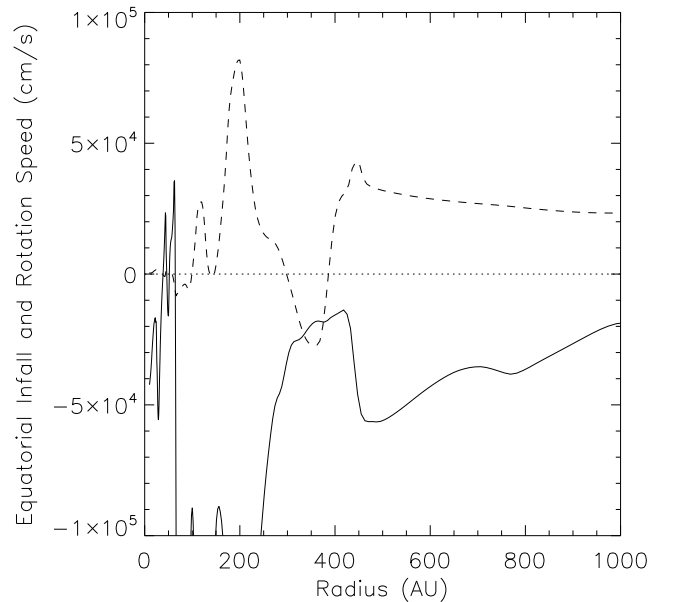


**Figure 4.** Equatorial infall  $v_r$  (solid line) and rotation  $v_\phi$  (dashed) for the MHD model with classic resistivity, showing the lack of a rotationally supported disk. Note the counter-rotation inside 400 AU, with rotation speed often decreasing (rather than increasing) toward the origin. The spikes of positive radial velocity at  $\sim 50$  are related to episodic reconnection events.

explain the 11-year sunspot cycle (Parker 2007, §9.3). Large anomalous resistivity may also exist in star-

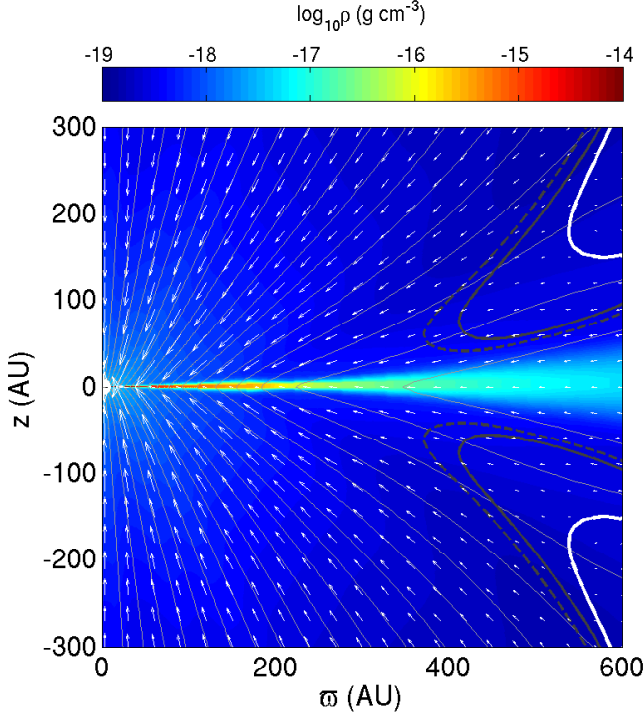


**Figure 5.** Same as Figures 1 and 2 but for Model ER18 with an enhanced resistivity  $\eta = 10^{18} \text{ cm}^2 \text{ s}^{-1}$ .

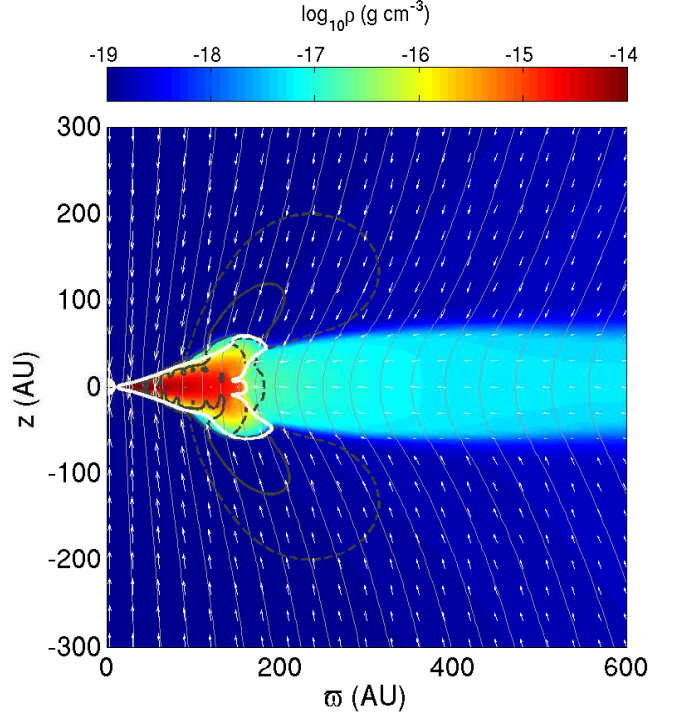


**Figure 7.** Same as Figures 1 and 2 but for Model ER20 with an enhanced resistivity  $\eta = 10^{20} \text{ cm}^2 \text{ s}^{-1}$ .

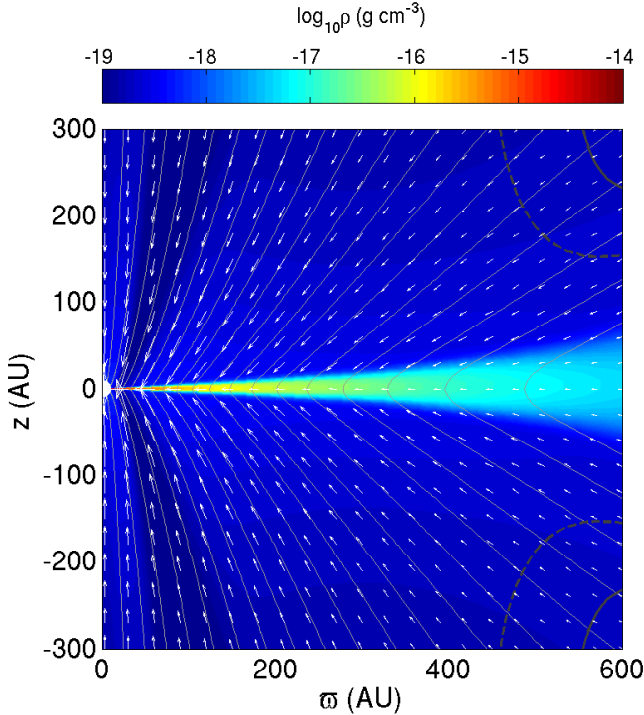


**Figure 6.** Same as Figures 1 and 2 but for Model ER19 with an enhanced resistivity  $\eta = 10^{19} \text{ cm}^2 \text{ s}^{-1}$ .

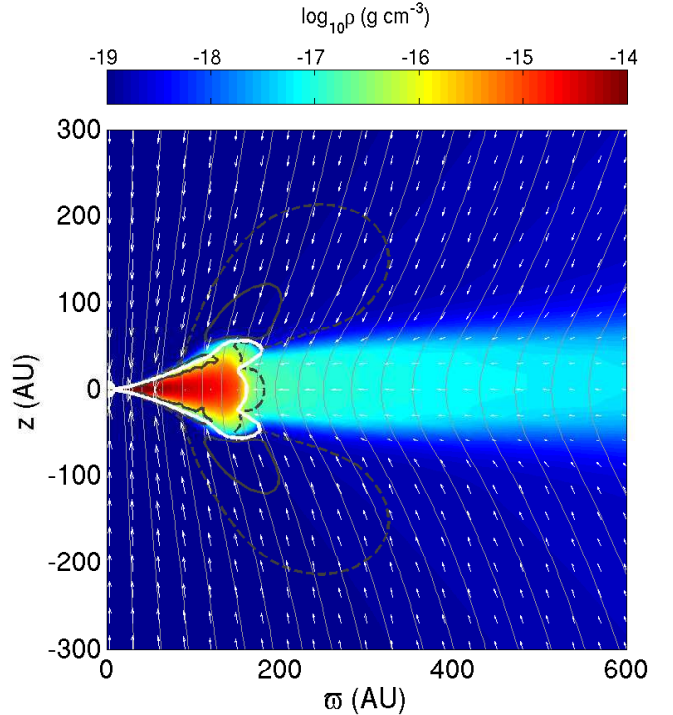


**Figure 8.** Same as Figure 7, with reduced space resolution.

forming molecular cloud cores at high densities (Norman & Heyvaerts 1985), although its magnitude is uncertain. Here we consider the simplest case of a spatially uniform resistivity of a range of values and for two different magnetic strength  $B_0 = 35.4$  and  $10.6 \mu\text{G}$ . The models

are summarized, together with the ones discussed earlier, in Table 1. We will concentrate on three representative, stronger field ( $B_0 = 35.4 \mu\text{G}$ ) models with  $\eta = 10^{18}$  (Model ER18),  $10^{19}$  (ER19), and  $10^{20} \text{ cm}^2 \text{ s}^{-1}$  (ER20), respectively. The weaker field models yield qualitatively

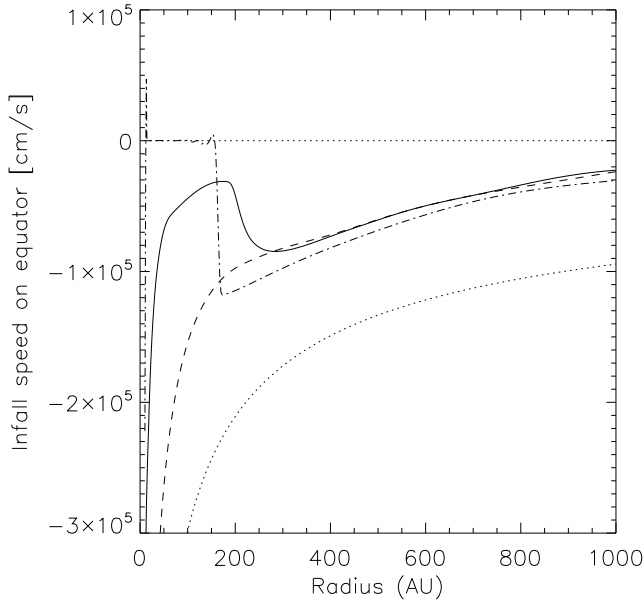


**Figure 9.** Equatorial infall speed for Model ER18 ( $\eta = 10^{18} \text{ cm}^2 \text{ s}^{-1}$ , solid line), ER19 ( $\eta = 10^{19} \text{ cm}^2 \text{ s}^{-1}$ , dashed), and ER20 ( $\eta = 10^{20} \text{ cm}^2 \text{ s}^{-1}$ , dash-dotted line) at the representative time  $t = 10^{12} \text{ s}$ . The free-fall speed is plotted as the lower dotted line for comparison.

similar results, and will be discussed briefly toward the end of the section.

Figures 5–7 show snapshots of the three models with enhanced resistivity, and Figures 9–11 display their infall and rotation speeds and vertical field strength on the equator. Additionally, Figure 8 shows the effect on Model ER20 of reducing numerical resolution by a factor of 2 in both  $r$  and  $\theta$ . Compared to the models without resistivity (Model HD shown in Figure 1) and with the classic resistivity (Model CR, Figure 3), the mass distribution and velocity field are much smoother, indicating that the enhanced resistivity in these models has largely eliminated the numerical reconnection. The suppression facilitates quantitative analysis of the simulations.

The mass distributions in the two lower resistivity models (Models ER18 and ER19) appear similar. Both have a dense equatorial region sandwiched from above and below by a more diffuse infalling envelope. The infall in the inner part of the envelope (within a few hundred AUs) appears to be guided by the field lines. It strikes the surfaces of the dense equatorial structure at a supersonic speed, forming two “accretion shocks.” These are reminiscent of the classic accretion shocks around Keplerian disks formed in non-magnetic simulations (e.g., Bodenheimer et al. 1990; see Figure 1). Their production is due, however, mainly to the magnetic field rather than rotation. Indeed, the same shocks form even in the absence of any rotation. For this reason, we will term these shocks “the magnetically induced accretion shocks.” They surround a magnetically induced “pseudodisk” (Galli & Shu 1993) rather than a rotationally supported Keplerian disk.

Figure 9 shows that the dense equatorial structure in Models ER18 and ER19 contains a pseudodisk rather than a rotationally supported disk. In both cases, the

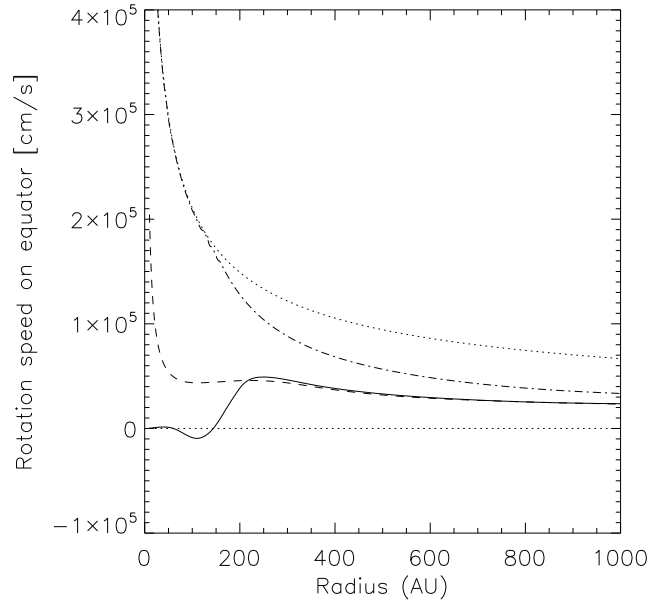


**Figure 10.** Same as Figure 9 but for the equatorial rotation speed. The Keplerian speed is plotted as the upper dotted line for comparison.

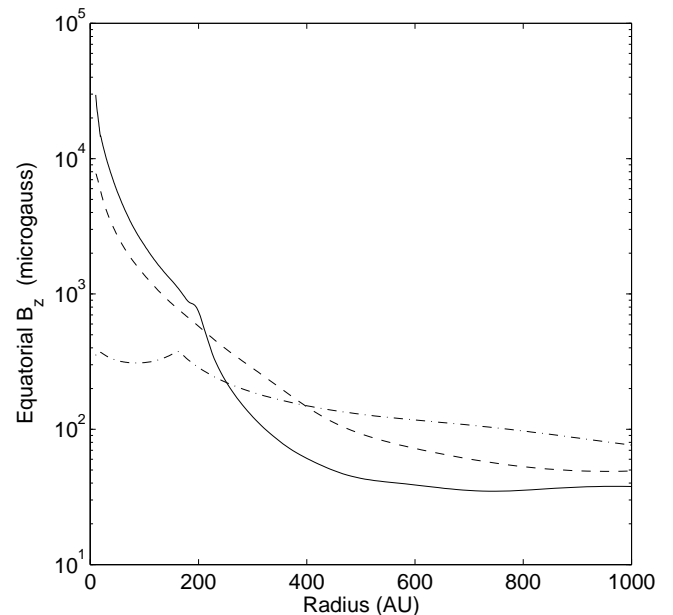


**Figure 11.** Same as Figure 9 but for the vertical magnetic field component  $B_z = -B_\theta$  on the equator.

infall is supersonic ( $> 2 \times 10^4 \text{ cm s}^{-1}$ ) within  $10^3 \text{ AU}$  of the central object, although there is significant difference in the infall speed within  $\sim 200 \text{ AU}$ : the equatorial material in the less resistive model ER18 falls inward more slowly than that in the more resistive model ER19. The prominent deceleration of infalling material around  $\sim 200 \text{ AU}$  in Model ER18 is reminiscent of the ambipolar diffusion-induced C-shock (or C-transition) first discussed in Li & McKee (1996; see also Ciolek & Königl 1998; Li 1999; Krasnopolsky & Königl 2002; Tassis & Mouschovias 2007 and especially Figure 3 of Mellon &

Li 2009). The physical origin is also similar. Just as ambipolar diffusion, the ohmic dissipation enables the field lines to diffuse relative to the material that plunges into the central object. The net effect is the formation of a strong (poloidal) field region at small radii, where the inward advection of the field lines by infalling material is balanced by the resistivity-induced outward magnetic diffusion. A relatively small resistivity such as that in Model ER18 allows for relatively larger magnetic gradients and Lorentz forces, which decelerate the infalling material more strongly. When the resistivity is small, the magnetic field remains a significant barrier to proto-stellar accretion.

The magnetic barrier weakens as the resistivity increases. In Model ER19, which is ten times more resistive than Model ER18, the ohmic dissipation-induced deceleration has all but disappeared. This is because the higher resistivity can support only a smaller current, making it hard to effectively “trap” the magnetic flux that is dragged to the small radii by the collapsing flow. Nevertheless, the infall speed is considerably smaller (by about a factor of two or so) than the free-fall speed, which is also plotted in Figure 9 for comparison. The sub-free-fall motion comes about because the equatorial infall is retarded by a combination of centrifugal and magnetic forces, although the magnetic forces appear to be the more important contributor, since the rotation speed shown in Figure 10 is about 1/3 of the Keplerian speed or less (yielding a centrifugal force an order of magnitude weaker than the gravity).

Note from Figure 10, for the least resistive model ER18, the equatorial rotation speed within  $\sim 200$  AU of the origin decreases, rather than increases, toward the center. Obviously, the decrease is due to magnetic braking, which is apparently so efficient as to produce a region of counter-rotation at  $\sim 100$  AU. The counter rotation is reminiscent of the case of magnetized core collapse in the presence of ambipolar diffusion with a relatively high cosmic ray ionization rate  $10^{-16} \text{ s}^{-1}$  studied by Mellon & Li (2009; see the bottom panel of their Figure 4). In both cases, the efficient braking is due to the strong poloidal field trapped by infall at the small radii. It removes essentially all of the angular momentum of the equatorial material that crosses the inner boundary of the computation domain. In the more resistive model ER19, the equatorial rotation speed inside  $\sim 200$  AU is initially kept nearly constant, before increasing rapidly. The peak rotation speed remains well below the local Keplerian speed, indicating that a rotationally supported disk is not formed. We conclude that the dense, flattened, equatorial structure produced in both Models ER18 and ER19 feature dense pseudodisks, but no rotationally supported dense disks. These pseudodisks are thinner than the Keplerian disk shown in Figure 1 for the hydro case because of vertical compression by pinched field lines, and smaller column densities (due to the fast infall rate inside the pseudodisk), corresponding to reduced scale height for a given gas density. The absence of a rotationally supported disk in these two cases (which have resistivities much larger than the classical value) supports our results in §2.2 and 3 that disk formation is suppressed by magnetic braking in the ideal MHD limit and in the presence of the classical resistivity, even though these results were affected by numerical reconnection.

The most resistive model ER20 differs drastically from the lower resistivity cases. It produces a much denser disk of radius  $\sim 150$  AU at the representative time  $t = 10^{12} \text{ s}$  (see Figure 7), which turns out to be rotationally supported. The strongest evidence for rotational support comes from Figure 10, which shows that the rotation speed at the equator is nearly identical to the Keplerian speed inside  $\sim 150$  AU. The support is also evident in Figure 9, which shows that the infall has nearly stopped at small radii (the spike near the inner edge of the computation grid is likely related to the outflow boundary condition, which is not ideal for a rotationally supported disk; it was present in the hydro case as well). The thick dashed and solid dark gray lines in Figure 7, which mark the location of  $|v_\phi| = 0.9 v_K$  and  $v_K$ , respectively, also make the case. The disk has a mass  $\sim 0.01 M_\odot$  at  $t = 10^{12} \text{ s}$ , corresponding to an average accretion rate (from the envelope to the disk)  $\sim 5 \times 10^{-7} M_\odot \text{ yr}^{-1}$ . As in the pure hydro case (§2.1), little of the disk material passes through the disk onto the central object in our axisymmetric simulations. Gravitational torques may be needed to drive the further evolution of such disks (in three dimensions).

Another feature of Model ER20 is that the poloidal field lines pass through the equatorial region with only a moderate bending. It is of course a consequence of the large resistivity, which allows the field lines to diffuse outward easily relative to the infalling material. This is especially true inside the inner, Keplerian disk, where the combination of slow radial motion and large resistivity means that the magnetic field must be nearly vertical and uniform (see the dot-dashed line in Figure 11). A consequence of the nearly uniform field is that there is little vertical compression by the magnetic field, yielding a Keplerian disk that is thicker than the magnetically compressed pseudodisks in the less resistive models (see Figures 5 and 6).

Outside the Keplerian disk lies a supersonically infalling pseudodisk. It is linked to the surrounding envelope by magnetic field lines; they are separated by the magnetically induced accretion shocks. Upstream of the shock, the low density envelope collapses more or less along the field lines, indicating that flux-freezing is approximately valid, because the field lines there are relatively straight and there is little current to be dissipated by the (large) resistivity. Downstream of the shock, the dense pseudodisk collapses horizontally, nearly perpendicular to the (poloidal) field lines. At the relatively late time shown in Figure 7, the field lines inside the pseudodisk are nearly held fixed in space, with the inward advection due to infalling material balanced by the outward resistivity-driven diffusion.

The role of resistivity in enabling disk formation can be seen clearly in Figure 11, where the vertical component of the magnetic field on the equator,  $B_z$ , is plotted as a function of time for all three models with different enhanced resistivities. The equatorial infall in the pseudodisk tends to compress the poloidal field lines, leading to a sharp increase in the poloidal field strength at small radii. Resistivity, on the other hand, tends to smooth out the field distribution. The net effect is that the poloidal field strength at small radii depends strongly on the magnitude of the resistivity, being larger for smaller resistivities. Since most of the magnetic braking occurs at rela-



tively small radii, where the infalling material attempts to spin up the fastest to conserve angular momentum, the stronger poloidal fields in the two less resistive cases (models ER18 and ER19) produce a stronger braking, which is enough to suppress the formation of a rotationally supported disk. The most resistive case (model ER20) has the weakest poloidal field at small radii (where magnetic braking matters most in the model) which, together with a large slippage between the field lines and matter in the azimuthal direction (which makes it hard to generate a toroidal field), makes the magnetic braking ineffective and disk formation possible. That the disk in model ER20 forms as a result of enhanced resistivity rather than numerical diffusion is supported by the fact that a nearly identical disk is formed in the lower resolution run (see Figure 8).

One can roughly estimate the size of the resistivity-enabled disk as follows. In order for the formed rotationally supported disk to survive against magnetic braking, the disk rotation must not twist up the poloidal magnetic field that threads the disk too strongly. This is satisfied when the magnetic diffusion speed becomes comparable to the Keplerian speed, which leads to the condition  $\eta \sim v_K H$ , where  $H$  is the vertical scale length over which the toroidal magnetic field varies. If we take  $H$  to be the disk pressure scale height (ignoring possible magnetic compression of the disk), and use the standard result for a thin-disk  $H/r \sim a/v_K$  (where  $r$  is the radius and  $a$  is the isothermal sound speed), then  $\eta \sim ra$  or  $r \sim \eta/a \sim 3.3 \times 10^2$  AU (for  $\eta = 10^{20} \text{ cm}^2 \text{ s}^{-1}$  and  $a = 2 \times 10^4 \text{ cm s}^{-1}$ ). This is about a factor of two larger than the disk radius that we found numerically in Figure 7. We should caution the reader that the above estimate did not take into account the detailed magnetic geometry and braking efficiency, which depends on the field strength (see below). For a weak enough field, a disk can form independent of the magnitude of the resistivity.

Besides the three representative models discussed above, we have carried out two additional simulations with  $\eta = 3 \times 10^{18}$  (Model ER18.5) and  $3 \times 10^{19} \text{ cm}^2 \text{ s}^{-1}$  (Model ER19.5). As one would expect based on the results for Models ER18 and ER19, no rotationally supported disk forms in Model ER18.5. There is a small ( $\sim 40$  AU in radius) rotationally supported disk in the more resistive Model ER19.5 at the fiducial time  $t = 10^{12}$  s. The disk shrinks with time, however. By  $t = 2 \times 10^{12}$  s, its radius decreases to  $\sim 25$  AU; it may disappear altogether at a later time. The trend indicates that  $\eta = 3 \times 10^{19} \text{ cm}^2 \text{ s}^{-1}$  is probably close to the critical resistivity  $\eta_c$  needed for disk formation.

The value for the critical resistivity  $\eta_c$  depends on the initial field strength  $B_0$ . This is to be expected since, in the limit of infinitely weak field, rotationally supported disks can form without any (enhanced) resistivity at all (i.e.,  $\eta_c = 0$ ). For a moderately magnetized dense core of  $B_0 = 10.6 \mu\text{G}$ , we find that the transition between the formation of a rotationally support disk and its suppression occurs between  $\eta = 10^{18}$  (Model ER18w) and  $3 \times 10^{18} \text{ cm}^2 \text{ s}^{-1}$  (Model ER18.5w). This value of  $B_0$  is probably close to the lower limit to the field strength in dense cores, judging from the fact that the median field strength for the more diffuse, cold neutral medium (CNM) of atomic gas is  $\sim 6 \mu\text{G}$  (Heiles & Troland 2005)

and that the directly measured line-of-sight component of the magnetic fields in a number of dense cores is of this order or higher (Crutcher & Troland 2008); the full strength of the core magnetic field is likely significantly higher. It is therefore reasonable to expect the critical value  $\eta_c$  for disk formation in cloud cores magnetized to a realistic level to lie somewhat between  $\eta_c \sim 3 \times 10^{18}$  and  $\sim 3 \times 10^{19} \text{ cm}^2 \text{ s}^{-1}$ . In what follows, we will take  $\eta_c = 10^{19} \text{ cm}^2 \text{ s}^{-1}$  as the characteristic critical value, with the understanding that it depends somewhat on the field strength, and can be uncertain by a factor of  $\sim 3$  in either direction.

## 5. DISCUSSION AND CONCLUSION

Our most important result is that classical resistivity alone appears unable to weaken magnetic braking enough to allow a rotationally supported disk to form for a realistic level of core magnetization, and that an enhanced resistivity of order  $\eta_c = 10^{19} \text{ cm}^2 \text{ s}^{-1}$  is needed.

A large, enhanced resistivity (of order  $2 \times 10^{20} \text{ cm}^2 \text{ s}^{-1}$ ) was advocated by Shu et al. (2006) to solve the so-called “magnetic flux problem” in star formation. They introduced the concept of the Ohm sphere, with a radius:

$$r_{\text{Ohm}} = \frac{\eta^2}{2GM_*} \quad (11)$$

where  $M_*$  is the central stellar mass. It can be obtained by setting the characteristic magnetic diffusion speed  $v_d = \eta/r$  equal to the free-fall speed  $v_{\text{ff}} = (2GM_*/r)^{1/2}$ . In the limit of a weak magnetic field (so that the magnetic forces do not affect the accretion dynamics) and zero rotation, Shu et al. (2006) showed that the magnetic field becomes more or less uniform inside the Ohm sphere; the sphere may be thus regarded as the region of complete magnetic decoupling. If a rotationally supported disk were to form inside the Ohm sphere, it would be protected against strong braking by the decoupling.

If the Ohm sphere must be larger than the rotationally supported disk, then to form a disk of  $10^2$  AU in radius around a half-solar mass star, the resistivity must be  $\eta_0 = \sqrt{2GM_* r_d} \sim 4.5 \times 10^{20} \text{ cm}^2 \text{ s}^{-1}$ . Our actual, numerically obtained, value of resistivity for disk formation is one to two orders of magnitude smaller, depending on the magnetic field strength. The discrepancy indicates that the simple considerations leading to the Ohm sphere need to be modified. One such modification is that the (radial) magnetic diffusion speed  $v_d$  is expected to be larger than  $\eta/r$ , because the field lines bend sharply inside the pseudodisk, with a field variation scale  $\Delta$  much less than  $r$  (see Figs. 5 and 6). The other is that the infall speed can be significantly below the free-fall value (see Fig. 9). Both modifications make it easier for the field lines to diffuse out, lowering the critical value for disk formation compared with the simple estimate based on the concept of Ohm sphere.

Nevertheless, the critical resistivity for disk formation is still a few orders of magnitude higher than the classical value. How such an enhanced resistivity may arise is unclear (see Parker 1979). One possibility is turbulent resistivity, which has been discussed, for example, in the context of magnetized accretion disks (e.g., Lubow, Papaloizou, & Pringle 1994; Guan & Gammie 2009). There are at least two possible origins for turbulence on the disk

formation scale (of  $10^2$ – $10^3$  AU). First, the dense cores that collapse into stars are observed to have non-thermal motions on the tens of thousands of AU scale, which can be interpreted as a subsonic turbulence of order half the sound speed (Bergin & Tafalla 2007). It is likely that the turbulent motions would continue down to smaller scales as the core collapses. Second, the collapsing flow can be significantly retarded by magnetic forces (see, e.g., the infall speed for Model ER18 in Figure 9). The magnetic support of the collapsing material against gravity may lead to interchange instability in 3D, which could develop into a turbulence, and might itself lead to an effective turbulent resistivity. Whether turbulent resistivity can enable the formation of rotationally supported disks or not requires high-resolution 3D simulations, perhaps along the line of Kowal et al. (2009). Another possibility is anomalous resistivity associated with, for example, current-driven instabilities (Norman & Heyvaerts 1985). Whether these and other enhancements of resistivity can enable disk formation remains to be determined. If not, other means of enabling disk formation, such as the Hall effect and outflow stripping of the protostellar envelope, need to be explored.

Although our idealized calculations indicate that a considerable enhancement in resistivity is needed if ohmic dissipation alone is to enable the formation of rotationally supported disks during the protostellar accretion phase of low-mass star formation, the exact value for the required enhancement is uncertain, and can be better determined with future refinements. One refinement is to include the self-gravity, which would also allow us to follow the formation and evolution of the dense magnetized core to the point of point-mass formation. The prestellar core evolution would provide a more self-consistent initial condition for the disk formation calculation during the protostellar accretion phase. An integrated treatment of both core formation and protostellar accretion may enable us to determine the distribution of the matter surrounding the dense core, which can aid the core material in removing the angular momentum from the forming disk, especially if the core is highly flattened along the field lines (Basu & Mouschovias 1994; Krasnopolsky & Königl 2002; see e.g., Tassis et al. 2009 for statistical evidence of core flattening). Another refinement, which we plan to do, is to study the combined effect of resistivity and ambipolar diffusion on disk formation. In addition, it would be desirable to find a better way to quantify the numerical reconnection, originated physically from the strong collapse-induced magnetic pinching, that affects the ideal MHD and low resistivity simulations. We conclude that how protostellar disks form around accreting protostars remains a mystery.

We acknowledge support by the Theoretical Institute for Advanced Research in Astrophysics (TIARA), and by the National Science Council of Taiwan through grant NSC97-2112-M-001-018-MY3. This work is supported in part by NASA ATP (NNG06GJ33G) and Origins grants. We acknowledge useful conversations with Roger Blandford, Arieh Königl, Chris McKee, Jon McKinney, Nir Shaviv, and Ron Taam.

## REFERENCES

- Allen, A., Li, Z.-Y., & Shu, F. H. 2003, *ApJ*, 599, 363  
 André, P., Ward-Thompson, D., & Barsony, M. 2000, in *Protostars and Planets IV*, ed. V. Mannings, A. P. Boss, & S. S. Russell (Tucson: Univ. of Arizona), p. 59  
 Banerjee, R., & Pudritz, R. E. 2006, *ApJ*, 641, 949  
 Basu, S., & Mouschovias, T. Ch. 1994, *ApJ*, 432, 720  
 Basu, S., & Mouschovias, T. Ch. 1995, *ApJ*, 452, 386  
 Bergin, E. A., & Tafalla, M. 2007, *ARA&A*, 45, 339  
 Bodenheimer, P. 1995, *ARA&A*, 33, 199  
 Bodenheimer, P., Yorke, H. W., Rozyczka, M., Tohline, J. E. 1990, *ApJ*, 355, 651  
 Ciolek, G. E., & Königl, A. 1998, *ApJ*, 504, 257  
 Clarke, D. A., Norman, M. L., & Fiedler, R. A. 1994, *ZEUS-3D User Manual* (Tech. Rep. 015; Urbana-Champaign: National Center for Supercomputing Applications)  
 Crutcher, R. M., & Troland, T. H. 2008, *ApJ*, 685, 281  
 Draine, B. T., Roberge, W. G., & Dalgarno, A. 1983, *ApJ*, 264, 485  
 Duffin, D. F., & Pudritz, R. E. 2009, *ApJ*, 706, L46  
 Enoch, M. L., Corder, S., Dunham, M. M., & Duchêne, G. 2009, *ApJ*, 707, 103  
 Evans, N. J., et al. 2009, *ApJS*, 181, 321  
 Fendt, C., & Čemeljić, M. 2002, *A&A*, 395, 1045  
 Fleming, T. P., Stone, J. M., & Hawley, J. F. 2000, *ApJ*, 530, 464  
 Galli, D., Lizano, S., Shu, F. H., & Allen, A. 2006, *ApJ*, 647, 374  
 Galli, D., & Shu, F. H. 1993, *ApJ*, 417, 220  
 Goodman, A. A., Benson P. J., Fuller G. A., & Myers P. C. 1993, *ApJ*, 406, 528  
 Guan, X., & Gammie, C. F. 2009, *ApJ*, 697, 1901  
 Heiles, C., & Troland, T. H. 2005, *ApJ*, 624, 773  
 Hennebelle, P., & Ciardi, A. 2009, *A&A*, 506, L29  
 Hennebelle, P., & Fromang, S. 2008, *A&A*, 477, 9  
 Hosking, J. G., & Whitworth, A. P. 2004, *MNRAS*, 347, 1001  
 Jørgensen, J. K., Bourke, T. L., Myers, P. C., Di Francesco, J., van Dishoeck, E. F., Lee, C.-F., Ohashi, N., Schöier, F. L., Takakuwa, S., Wilner, D. J., & Zhang, Q. 2007, *ApJ*, 659, 479  
 Kowal, G., Lazarian, A., Vishniac, E. T., & Otmianowska-Mazur, K. 2009, *ApJ*, 700, 63  
 Krasnopolsky, R., & Königl, A. 2002, *ApJ*, 580, 987  
 Krasnopolsky, R., Li, Z.-Y., & Blandford, R. 1999, *ApJ*, 526, 631  
 Krasnopolsky, R., Li, Z.-Y., & Blandford, R. 2003, *ApJ*, 595, 631  
 Li, Z.-Y. 1999, *ApJ*, 497, 850  
 Li, Z.-Y., & McKee, C. F. 1996, *ApJ*, 464, 373  
 Lubow, S. H., Papaloizou, J. C. B., & Pringle, J. E. 1994, *MNRAS*, 267, 235  
 Machida, M. N., Matsumoto, T., Tomisaka, K., Hanawa T. 2005, *MNRAS*, 362, 369  
 Mathis, J. S., Rumpl, W., & Nordsieck, K. H. 1977, *ApJ*, 217, 425  
 Mellon, R. R., & Li, Z.-Y. 2008, *ApJ*, 681, 1356  
 Mellon, R. R., & Li, Z.-Y. 2009, *ApJ*, 698, 922  
 Miller, K. A., & Stone, J. M. 1997, *ApJ*, 489, 890  
 Nakano, T., Nishi, R., & Umebayashi, T. (2002) *ApJ*, 573, 199  
 Norman, C., & Heyvaerts, J. 1985, *ApJ*, 147, 247  
 Parker, E. N. 1979, *Cosmical Magnetic Fields: Their Origin and Their Activity* (Oxford: Clarendon)  
 Parker, E. N. 2007, *Conversations on Electric and Magnetic Fields in the Cosmos* (Princeton: Princeton Univ. Press)  
 Pinto, C., & Galli, D. 2008, *A&A*, 484, 17  
 Price, D. J., & Bate, M. R. 2007, *Ap&SS*, 311, 75  
 Sano, T., Miyama, S. M., Umebayashi, T., Nakano, T. 2000, *ApJ*, 543, 486  
 Shu, F. H., Adams, F. C., & Lizano, S. 1987, *ARA&A*, 25, 23  
 Shu, F. H., Galli, D., Lizano, D., & Cai, M. 2006, *ApJ*, 647, 382  
 Tassis, K., Dowell, C. D., Hildebrand, R. H., Kirby, L., & Vaillancourt, J. E. 2009, *MNRAS*, 399, 1681  
 Tassis, K., & Mouschovias, T. Ch. 2007, *ApJ*, 660, 370  
 Troland, T. H., & Crutcher, R. M. 2008, *ApJ*, 680, 457  
 Ulrich, R. K. 1976, *ApJ*, 210, 377  
 Umebayashi, T., & Nakano, T. 1990, *MNRAS*, 243, 103  
 van Dishoeck, E. F., & Jørgensen, J. K. 2008, *Ap&SS*, 313, 15  
 Wardle, M., & Ng, C. 1999, *MNRAS*, 303, 239